Indirect measurement of infrared absorption spectrum through thermal emission of meta-cavity array

QIONG QIONG CHU, FENG YUAN ZHANG, YE ZHANG, SHI NING ZHU, AND HUI LIU[*]

National Laboratory of Solid State Microstructures, School of Physics, Collaborative Innovation Center of Advanced Microstructures, Nanjing University, Nanjing, Jiangsu 210093, China
[*]*liuhui@nju.edu.cn*

Abstract: Controlling thermal emission is essential for various infrared spectroscopy applications. Metasurfaces can be utilized to control multiple degrees of freedom of thermal emission, enabling the compact thermal emission materials and devices. Infrared spectroscopy such as FTIR (Fourier transform infrared spectroscopy), usually requires external infrared radiation source and complex spectroscopic devices for absorption spectrum measurement, which hinders the implementation of integrated compact and portable measurement equipment. Measuring absorption spectrum through the thermal emission of pixelated thermal emitter array can facilitate the integration and miniaturization of measurement setup, which is highly demanded for on-chip spectroscopy applications. Here, we experimentally demonstrate an integrated technology that allows for indirect measurement of the absorption spectrum through the thermal emission of meta-cavity array. This indirect measurement method opens a new avenue for compact infrared spectroscopy analysis.

1. Introduction

The control of thermal emission is important for the development of various infrared applications, such as thermophotovoltaic device [1–3], heat management [4–6], thermal camouflage [7,8], radiative cooling [9–12], infrared radiation source [13,14] and so on. Metasurfaces, as an effective way to manipulate multiple degrees of freedom of optical waves, have been widely investigated for many applications, such as meta-lens [15,16], biosensors [17–19] and perfect absorbers [20,21]. In recent years, metasurface based thermal emitters [22–36] have attracted tremendous attention due to their remarkable capability to tune thermal emission with multiple degrees of freedom, such as wavelengths [37], polarizations [38], radiation angles [39], bandwidth [40] and spatial radiation patterns [41]. Through metasurface array, pixelated thermal emitters [42] can further enable the integration of multifunctional infrared devices, such as spectroscopy applications.

Infrared spectroscopy [43,44] is a common way to obtain the absorption spectrum through transmission T and reflection R spectrum measurement, as A = 1-T-R, which usually requires complex spectroscopic equipment and infrared radiation source during the measuring process. According to Kirchhoff's law, the emissivity of materials can be equivalent to their absorptivity under the thermal equilibrium condition. Utilizing single thermal emitter [45,46] as an infrared radiation source, the characteristic absorption bands of molecular can be detected through emission spectrum measurement while an infrared spectrometer or simplified spectroscopic equipment is needed. It is quite necessary to invent the integrated and compact absorption spectrum measurement technique without the need of an external infrared radiation source and infrared spectrometer. Through the thermal emission of pixelated thermal emitter array, it is possible to obtain the spectral absorption information from spatially distributed thermal emitter pixels. Indirect measurement of the infrared absorption spectrum can be realized without

requirement of external infrared radiation source and infrared spectrometer. This way can further realize the miniaturization and integration of measurement device.

In this work, we demonstrate a pixelated meta-cavity array to realize a thermal emission microchip with emission wavelengths covering 7.8-12 μm infrared range. Based on this microchip design and the thermal imaging approach, we propose a highly integrated indirect infrared absorption spectrum measurement technique without the need of external infrared radiation source and infrared spectrometer. Through the thermal imaging of the microchip with or without the polymer molecule layer, the equivalent absorption spectrum of polymer molecules can be indirectly obtained from the variations of thermal emission energy. On the basis of the pixelated meta-cavity array design, demonstrated absorption spectrum measurement technique enables the integration of the infrared radiation source and the spectroscopic chip, simplifying the measurement system and reducing the operating costs. Also, in the measuring process, the direct contact between the detected sample and the chip can be avoided. Benefiting from these advantages, this novel technique can find many potential applications based on compact infrared spectroscopy, such as organic molecular sensing and environment monitoring.

2. Theoretical analysis

2.1. Thermal emission microchip design

Here, a meta-cavity array based thermal emission microchip is designed with each meta-cavity pixel possessing one emission peak. By integrating meta-cavity pixels, this microchip can simultaneously perform as an integrated infrared radiation source and infrared spectrometer, providing pixelated spectroscopic analysis. Designed microchip is composed of a nanohole metasurface array, a gold mirror, and a dielectric Si layer sandwiched between them, as shown in Fig. 1(a). Each metasurface of meta-cavity is artificially designed to tune the FP mode to obtain desired resonant wavelength. Polarized nanohole designs are chosen because their resonant wavelengths can be continuously tuned as the nanohole length increases. Through continuously modulating the nanohole parameters, a multiband microchip can be realized. Specifically, the unit cell period along x axis and the width of nanoholes are fixed as Px = 1.6 μm, w = 0.2 μm. The length of nanoholes depends on the unit cell period along y axis, defined as L = Py*0.5. We set Py as 2, 2.2, 2.4, 2.6, 3, 3.4, 3.8, 4.2 and 4.6 μm respectively, corresponding to nine different metasurfaces. The thickness of Au/Si/Au layers is set as 70 nm/0.96 μm/100 nm. Simulated absorption spectra of the meta-cavity array under x-polarized incidence are shown in Fig. 1(c). We can see that with the increase of the nanohole length, linearly tunable resonant wavelengths covering 7.8-12 μm are achieved, thus enabling the realization of multiband infrared radiation source. In contrast, under y-polarized incidence, nanohole metasurfaces cannot be excited and the corresponding absorption (gray lines) is close to zero. This polarization-selective property can be flexibly tuned by manipulating the long-axis orientation of the nanoholes.

2.2. Equivalent absorptivity calculation

According to Kirchhoff's law, the thermal emissivity ε of meta-cavity pixels is equal to the absorptivity A under the thermal equilibrium condition. Therefore, we can obtain the thermal emissivity and corresponding thermal emission energy of each meta-cavity pixel through its absorption spectrum. By analyzing the thermal emission intensity change before and after the thermal emission signal of meta-cavity pixels passes through the absorptive layer above it, we can obtain the equivalent absorption spectrum of the detected absorptive layer. Specifically, the variations of the thermal emission intensity of meta-cavity pixels can be represented by the variations of their thermal emission energy. The thermal emission energy of meta-cavity pixels in infinitesimal wavelength intervals can be calculated as $PB_i = \varepsilon_i M_{bb}(\lambda_i, T)(\Delta\lambda_i)$ $(i = 1, 2, 3\ldots)$, where ε represents the emissivity of meta-cavity pixel, M_{bb} is the calculated blackbody emissivity
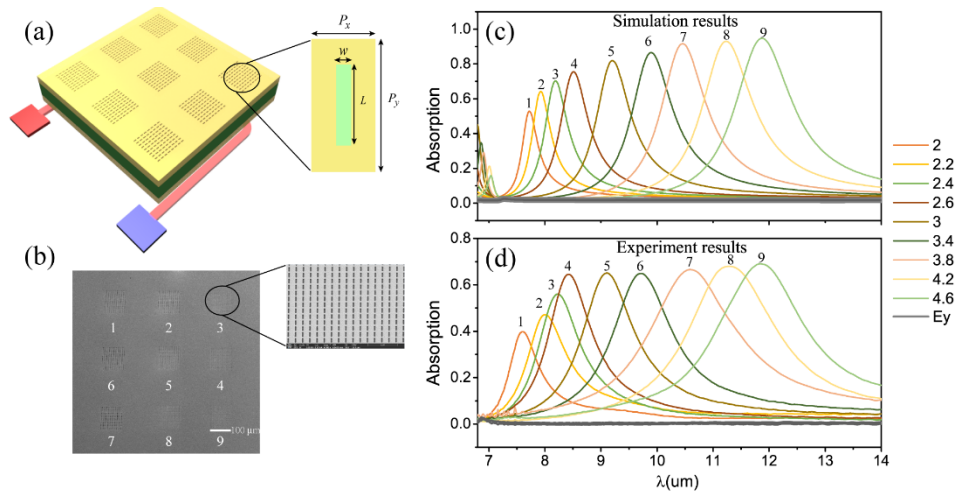
Fig. 1. Meta-cavity array based thermal emission microchip. (a) Sketch of designed thermal emission microchip. (b) Micrograph of fabricated meta-cavity array. The inset of (a) and (b) depict the unit cell of meta-cavity array and zoomed-in SEM image of fabricated meta-cavity. (c) Simulated absorption spectra of meta-cavity array under x-polarized incidence. The gray lines present the simulated absorption spectra of meta-cavity array under y-polarized incidence. (d) Measured absorption spectra of meta-cavity array.

according to Planck's law. T is the temperature of the microchip and i represents the number of the infinitesimal wavelength intervals. Next, when the absorptive layer is placed above the microchip, the thermal emission energy of meta-cavity pixels can be recalculated as $PB_i' = (1 - A_i - R_i)\varepsilon_i M_{bb}(\lambda_i, T)(\Delta\lambda_i)$ $(i = 1, 2, 3 \ldots)$. Here A_i and R_i represent the absorptivity and reflectivity of the absorptive layer. When the reflection of absorptive layer is negligible ($R_i \approx 0$), we can obtain the equivalent absorptivity by $A_i = 1 - PB_i'/PB_i$. Through combining the equivalent absorptivity of each meta-cavity pixel, the equivalent absorption spectrum of the absorptive layer can be obtained. It should be noted that the corresponding tendency of absorption spectrum can also be obtained even if there is some reflection at the interface of absorptive layer.

3. Experimental results and discussions

3.1. Infrared spectral properties of thermal emission microchip

In order to verify the wavelength-selective property of the designed thermal emission microchip, we fabricated the pixelated metasurface array on the top gold film through focused ion beam. Specifically, the etching depth of nanoholes is set as 70 nm. More fabrication details can be found in Supplement 1. Each metasurface of meta-cavity pixel is 100 μm × 100 μm sized and the SEM (scanning electron microscope) image of fabricated sample is displayed in Fig. 1(b). Through FTIR, we measured the absorption spectra of meta-cavity array under the excitation of x-polarized incidence at room temperature, as shown in Fig. 1(d). It can be seen that the experimental results agree well with the theoretical results. With the increase of period Py and the nanohole length L, the absorption peaks of meta-cavity array gradually red shift from 7.8 to 12 μm. This multi-resonance characteristic verifies the feasibility of designed microchip as a multiband and polarized infrared radiation source. In addition, the Q factor of the absorption peaks of meta-cavity array in experiments is lower than that of simulation results because of the inevitable errors caused in the fabrication process. The difference between measured absorption

spectra and simulated results of No.1 and No.4 meta-cavities is mainly caused by the broaden nanohole width in fabrication.

3.2. Absorption spectrum measuring of PDMS

Next, the infrared characteristics of the thermal emission microchip are investigated by utilizing a long-wave thermal camera (7.6-14 μm). The measurement system is composed of an electric heating stage and a thermal camera, as shown in Fig. 2. The stage can provide uniform heating for the microchip. An absorptive molecular layer is inserted between the microchip and the camera by a rotating robotic arm without direct contact with the microchip. The thermal emission signal from the microchip, passing through the polymer layer, is detected by the thermal camera. Then, the thermal image is obtained for analysis. Reasonably, the vibrational information of detected molecular is encoded into the thermal images, as shown in the Fig. 2. It should be noted that the microchip and the polymer layer possess independent emission properties due to different temperatures. Benefiting from the integrated infrared radiation source and spectroscopic chip, the measurement system provides new insights for the design of on-chip infrared spectroscopy devices.
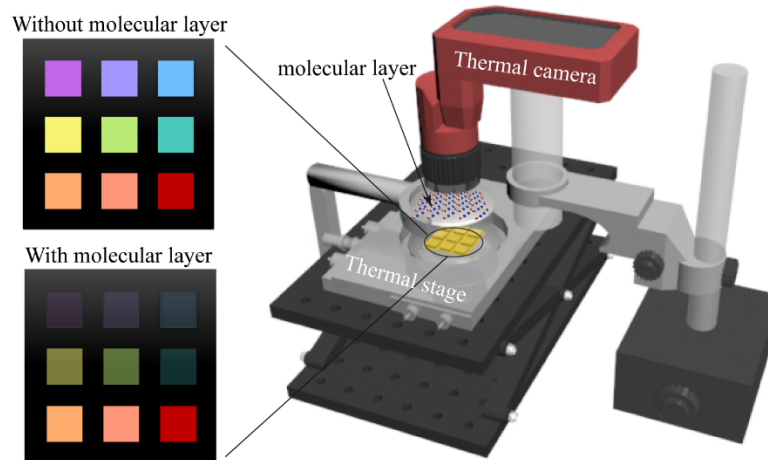

Fig. 2. Schematic diagram of the absorption spectrum measurement setup. The vibrational information of detected molecular is encoded into the thermal images taken with or without the molecular layer. The false color of the meta-cavity pixels from violet to red represents the emission wavelengths from 7.8 to 12 μm.

Firstly, we choose the PDMS (polydimethylsiloxane) organic molecular as the absorptive layer to be detected. According to the Kirchhoff's law, the emission spectrum of PDMS was measured with FTIR and utilized as the standard absorption spectrum, as shown in Fig. 3(d). According to the imaging principle of the thermal camera, the emission temperature of meta-cavity pixels in the thermal imaging is proportional to their thermal emission energy. Correspondingly, we can investigate the thermal emission energy variations of meta-cavity pixels through their emission temperature variations in thermal imaging. Then, the experimental equivalent absorptivity of the molecular layer can be calculated as $A_i = 1 - Tem_i'/Tem_i$ where the Tem_i' (Tem_i) represents the emission temperature of meta-cavity pixels in the thermal image with (without) molecular layer. Measured reflection spectrum of PDMS layer can be found in Supplement 1. Low reflectivity of PDMS layer enables the feasibility for indirect measurement of absorption spectrum.

In the thermal imaging experiments, the temperature of microchip was raised to 100°C with an electric heating stage. Then two thermal images were taken without or with the PDMS layer, as
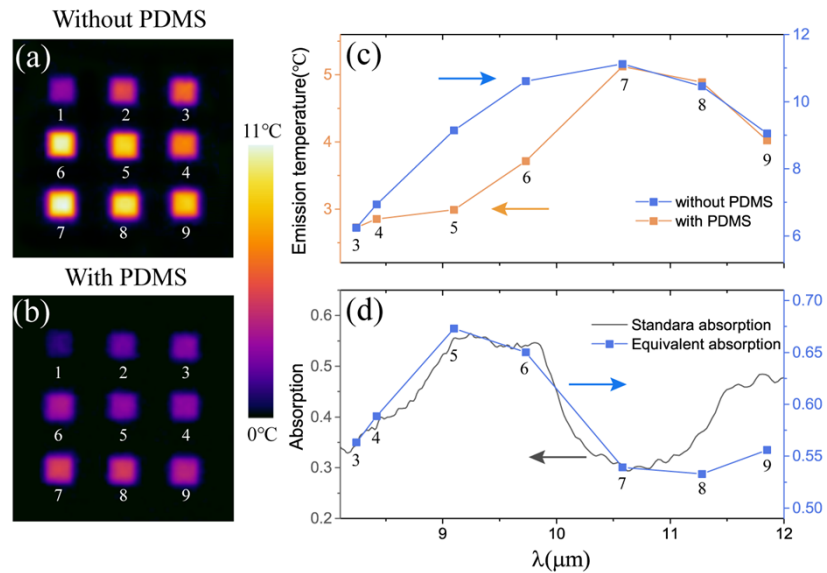
Fig. 3. Absorption spectrum measuring of PDMS. (a) The thermal image taken without molecular layer. (b) The thermal image taken with PDMS layer. (c) Measured emission temperature of meta-cavity pixels in thermal images with and without PDMS layer. (d) Standard absorption spectrum and the equivalent absorption spectrum of PDMS layer.

shown in Fig. 3(a, b), respectively. For the case without PDMS layer, the meta-cavity pixels with different emission capabilities display different emission temperatures in Fig. 3(a). For the case with PDMS layer in Fig. 3(b), the emission temperature of all meta-cavity pixels in the thermal image is reduced due to the molecular absorption. In order to obtain more accurate data, the average emission temperature *Tem′* and *Tem* of each meta-cavity pixel in two thermal images are extracted and given in Fig. 3(c). The area for averaging emission temperature is the area of fabricated nanohole metasurface of each meta-cavity. For clearly comparing the thermal emission difference of each meta-cavity pixel in the imaging, we set the average emission temperature of each meta-cavity pixel and its corresponding central emission wavelength as the y and x axis, respectively. Here, it should be noted that the emission temperature shown in the figure is the result after subtracting the background emission temperature (the emission temperature of metal surface around nanohole metasurfaces). Comparing the average emission temperature results in Fig. 3(a) and Fig. 3(b), it is clear that the emission temperature of No.5-6 meta-cavity pixels undergoes a significant decrease after the polymer layer is added. This means that the central emission wavelengths of No. 5-6 meta-cavity pixels equal to the absorption wavelengths of PDMS molecular. Comparing the two thermal images allows us to make an intuitive and quick measurement of the absorption spectrum of PDMS molecular. According to the derived emission temperature data of different meta-cavity pixels, we can obtain the experimental equivalent absorption spectrum of PDMS molecular without FTIR, as shown in Fig. 3(d). It can be seen that the equivalent absorption spectrum of PDMS is consistent with the standard absorption spectrum of PDMS measured with FTIR. Therefore, the absorption spectrum of PDMS molecular can be simply obtained from thermal imaging. In Fig. 3(d), the deviation between the experimental equivalent absorption spectrum and the standard absorption spectrum of PDMS mainly comes from the limited measured data due to the insufficient number of meta-cavity pixels. In the future, the measurement accuracy can be further improved through increasing the number of meta-cavity pixels. Furthermore, the absorptivity discrepancies between these two curves are mainly caused

by the different detectors and data processing programs. The reflection of the emitted signal from meta-cavity pixels at the molecular layer has very slight impact on the absorption spectrum.

3.3. Absorption spectrum measuring of ETFE, PTFE and PVDC

In order to demonstrate the universality of proposed imaging-based absorption spectrum measurement technique, we also detected three other types of organic molecular, ETFE (ethylene-tetra-fluoro-ethylene), PTFE (Poly-tetra-fluoroethylene) and PVDC (Polyvinylidene chloride), as shown in Fig. 4. Measured reflection spectra of those molecular layers can be found in Supplement 1. In Fig. 4(d), the emission temperature of No.1-7 meta-cavity pixels undergoes a significant decrease due to the absorption of molecular layer. Comparing with the standard absorption spectrum, the equivalent absorption spectrum of ETFE clearly shows the absorption bands in the same wavelength range (7.6-10.5 μm). In other two experiments of PTFE and PVDC, the emission temperature of No.2-5 meta-cavity pixels and No.5-6 meta-cavity pixels respectively undergo a clear decrease after adding the molecular layer, as shown in Fig. 4(e, f). The equivalent absorption spectra of PTFE and PVDC show the absorption bands of 7.6-9 μm and 9.2-9.8 μm respectively. These results are consistent with the absorption spectra measured with FTIR, verifying the feasibility and universality of this measurement method. More details can be found in Supplement 1. In our experiments, this simple repeatable measurement process can further improve the utilization and practicality of proposed absorption spectrum measurement technique.
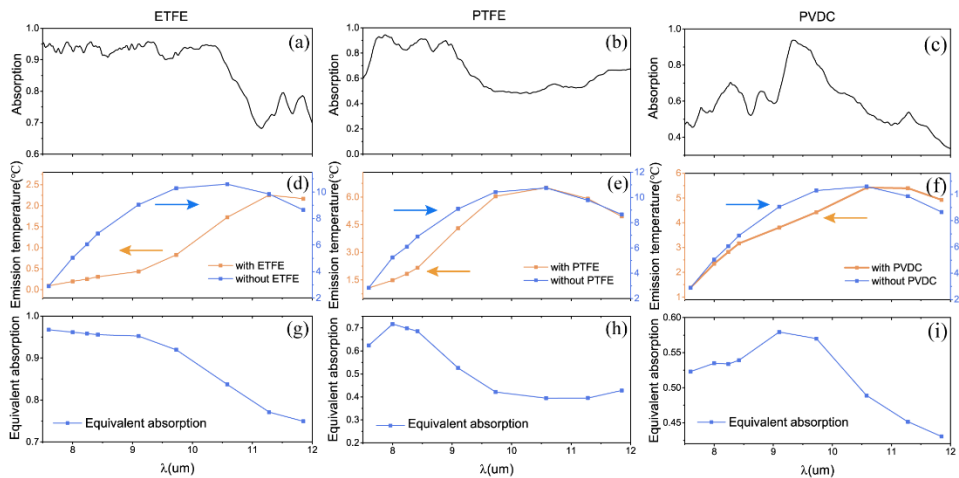

Fig. 4. Absorption spectrum measuring of ETFE, PTFE and PVDC. Absorption spectrum of molecular layer measured by FTIR (a-c); Measured emission temperature of meta-cavity pixels in thermal images with and without molecular layer (d-f); Equivalent absorption spectrum of molecular layer obtained from thermal imaging method (g-i).

It should be noted that the detection wavelength resolution is limited by the linewidth of the emission peaks of meta-cavity pixels due to metal ohmic loss in the long-wave infrared domain. For example, in Fig. 4(a), the vibrational modes of ETFE molecules with narrow linewidth near 11.5 μm cannot be detected in the experiment. In future, the wavelength resolution can be improved through integrating high-Q designs, such as a BIC array based on dielectric metasuface pixels. Based on above detection results, we can conclude that this imaging-based absorption spectrum measurement technique can efficiently and rapidly obtain the equivalent absorption spectrum of various organic molecular. In addition, thanks to the greatly simplified

measurement system, this integrated technique can be flexibly applied to many other compact infrared applications, such as integrated micro-molecular sensing and material analysis.

4. Conclusion

In summary, we proposed an integrated and compact technique to realize indirect infrared absorption spectrum measurement based on a pixelated meta-cavity array. By utilizing long-wave thermal camera, we can analyze the thermal emission of each meta-cavity pixel through thermal imaging with or without the absorptive layer. Then, the equivalent absorption spectrum of analyte compounds can be obtained when the reflection is negligible. In experiments, we have realized the absorption spectrum measurement of four kinds of molecules and the results are consistent with the absorption spectra obtained through FTIR. The designed thermal emission microchip can perform as an infrared radiation source and a spectroscopic chip simultaneously, realizing integrated compact on-chip absorption spectrum measurements. Although the wavelength resolution of this absorption spectrum measurement technique is limited due to ohmic loss in metal, future designs based on dielectric metasurfaces with less loss can be expected to improve it. This proposed imaging-based absorption spectrum measurement technique provides a potential technique for the miniaturization and integration of infrared applications, such as on-chip micro-molecular sensing, environmental monitoring and medical diagnosis.

Disclosures. The authors declare no conflicts of interest.

Data availability. Data underlying the results presented in this paper are not publicly available at this time but may be obtained from the authors upon reasonable request.

Supplemental document. See Supplement 1 for supporting content.

References

1. A. Lenert, D. M. Bierman, Y. Nam, W. R. Chan, I. Celanovic, M. Soljacic, and E. N. Wang, "A nanophotonic solar thermophotovoltaic device," Nat. Nanotechnol. **9**(2), 126–130 (2014).
2. J. Yang, W. Du, Y. S. Su, Y. Fu, S. X. Gong, S. L. He, and Y. G. Ma, "Observing of the super-Planckian near-field thermal radiation between graphene sheets," Nat. Commun. **9**(1), 4033 (2018).
3. D. J. Fan, T. Burger, S. McSherry, B. Lee, A. Lenert, and S. R. Forrest, "Near-perfect photon utilization in an air-bridge thermophotovoltaic cell," Nature **586**(7828), 237–241 (2020).
4. O. Ilic, P. Bermel, G. Chen, J. D. Joannopoulos, I. Celanovic, and M. Soljacic, "Tailoring high-temperature radiation and the resurrection of the incandescent source," Nat. Nanotechnol. **11**(4), 320–324 (2016).
5. R. St-Gelais, L. X. Zhu, S. H. Fan, and M. Lipson, "Near-field radiative heat transfer between parallel structures in the deep subwavelength regime," Nat. Nanotechnol. **11**(6), 515–519 (2016).
6. H. Yuan, H. Zhang, K. W. Huang, Y. Cheng, K. Wang, S. T. Cheng, W. J. Li, J. Jiang, J. L. Li, C. Tu, X. B. Wang, Y. Qi, and Z. F. Liu, "Dual-Emitter Graphene Glass Fiber Fabric for Radiant Heating," ACS Nano **16**(2), 2577–2584 (2022).
7. O. Salihoglu, H. B. Uzlu, O. Yakar, S. Aas, O. Balci, N. Kakenov, S. Balci, S. Olcum, S. Suzer, and C. Kocabas, "Graphene-Based Adaptive Thermal Camouflage," Nano Lett. **18**(7), 4541–4548 (2018).
8. Y. Li, X. Bai, T. Z. Yang, H. L. Luo, and C. W. Qiu, "Structured thermal surface for radiative camouflage," Nat. Commun. **9**(1), 273 (2018).
9. X. B. Yin, R. G. Yang, G. Tan, and S. H. Fan, "Terrestrial radiative cooling: Using the cold universe as a renewable and sustainable energy source," Science **370**(6518), 786–791 (2020).
10. D. Li, X. Liu, W. Li, Z. H. Lin, B. Zhu, Z. Z. Li, J. L. Li, B. Li, S. H. Fan, J. W. Xie, and J. Zhu, "Scalable and hierarchically designed polymer film as a selective thermal emitter for high-performance all-day radiative cooling," Nat. Nanotechnol. **16**(2), 153–158 (2021).
11. H. Z. Zhu, Q. Li, C. N. Tao, Y. Hong, Z. Q. Xu, W. D. Shen, S. Kaur, P. Ghosh, and M. Qiu, "Multispectral camouflage for infrared, visible, lasers and microwave with radiative cooling," Nat. Commun. **12**(1), 1805 (2021).
12. S. N. Zeng, S. J. Pian, M. Y. Su, *et al.*, "Hierarchical-morphology metafabric for scalable passive daytime radiative cooling," Science **373**(6555), 692–696 (2021).
13. X. Liu, Z. Li, Z. Wen, *et al.*, "Large-area, lithography-free, narrow-band and highly directional thermal emitter," Nanoscale **11**(42), 19742–19750 (2019).
14. Z.-Y. Yang, S. Ishii, T. Yokoyama, D. Thang Duy, M.-G. Sun, P. S. Pankin, I. V. Timofeev, T. Nagao, and K.-P. Chen, "Narrowband Wavelength Selective Thermal Emitters by Confined Tamm Plasmon Polaritons," ACS Photonics **4**(9), 2212–2219 (2017).

15. X. J. Ni, S. Ishii, A. V. Kildishev, and V. M. Shalaev, "Ultra-thin, planar, Babinet-inverted plasmonic metalenses," Light: Sci. Appl. **2**(4), e72 (2013).

16. S. M. Wang, P. C. Wu, V. C. Su, Y. C. Lai, M. K. Chen, H. Y. Kuo, B. H. Chen, Y. H. Chen, T. T. Huang, J. H. Wang, R. M. Lin, C. H. Kuan, T. Li, Z. L. Wang, S. N. Zhu, and D. P. Tsai, "A broadband achromatic metalens in the visible," Nat. Nanotechnol. **13**(3), 227–232 (2018).

17. G. Dayal, X. Y. Chin, C. Soci, and R. Singh, "High-Q Plasmonic Fano Resonance for Multiband Surface-Enhanced Infrared Absorption of Molecular Vibrational Sensing," Adv. Opt. Mater. **5**(2), 1600559 (2017).

18. F. Neubrech, C. Huck, K. Weber, A. Pucci, and H. Giessen, "Surface-Enhanced Infrared Spectroscopy Using Resonant Nanoantennas," Chem. Rev. **117**(7), 5110–5145 (2017).

19. A. John-Herpin, A. Tittl, L. Kühner, F. Richter, S. H. Huang, G. Shvets, S.-H. Oh, and H. Altug, "Metasurface-Enhanced Infrared Spectroscopy: An Abundance of Materials and Functionalities," Adv. Mater. **35**, 2110163 (2023).

20. Y. Yao, R. Shankar, M. A. Kats, Y. Song, J. Kong, M. Loncar, and F. Capasso, "Electrically Tunable Metasurface Perfect Absorbers for Ultrathin Mid-Infrared Optical Modulators," Nano Lett. **14**(11), 6526–6532 (2014).

21. Y. Li, J. Lin, H. Guo, W. Sun, S. Xiao, and L. Zhou, "A Tunable Metasurface with Switchable Functionalities: From Perfect Transparency to Perfect Absorption," Adv. Opt. Mater. **8**(6), 1901548 (2020).

22. H. T. Miyazaki, T. Kasaya, M. Iwanaga, B. Choi, Y. Sugimoto, and K. Sakoda, "Dual-band infrared metasurface thermal emitter for CO2 sensing," Appl. Phys. Lett. **105**(12), 121107 (2014).

23. D. Costantini, A. Lefebvre, A. L. Coutrot, I. Moldovan-Doyen, J. P. Hugonin, S. Boutami, F. Marquier, H. Benisty, and J. J. Greffet, "Plasmonic Metasurface for Directional and Frequency-Selective Thermal Emission," Phys. Rev. Appl. **4**(1), 014023 (2015).

24. M. Makhsiyan, P. Bouchon, J. Jaeck, J. L. Pelouard, and R. Haidar, "Shaping the spatial and spectral emissivity at the diffraction limit," Appl. Phys. Lett. **107**(25), 251103 (2015).

25. T. Yokoyama, T. D. Dao, K. Chen, S. Ishii, R. P. Sugavaneshwar, M. Kitajima, and T. Nagao, "Spectrally Selective Mid-Infrared Thermal Emission from Molybdenum Plasmonic Metamaterial Operated up to 1000 degrees C," Adv. Opt. Mater. **4**(12), 1987–1992 (2016).

26. C. Zou, G. Ren, M. M. Hossain, S. Nirantar, W. Withayachumnankul, T. Ahmed, M. Bhaskaran, S. Sriram, M. Gu, and C. Fumeaux, "Metal-Loaded Dielectric Resonator Metasurfaces for Radiative Cooling," Adv. Opt. Mater. **5**(20), 1700460 (2017).

27. W. Li and S. Fan, "Nanophotonic control of thermal radiation for energy applications," Opt. Express **26**(12), 15995–16021 (2018).

28. C.-C. Chang, W. J. M. Kort-Kamp, J. Nogan, T. S. Luk, A. K. Azad, A. J. Taylor, D. A. R. Dalvit, M. Sykora, and H.-T. Chen, "High-Temperature Refractory Metasurfaces for Solar Thermophotovoltaic Energy Harvesting," Nano Lett. **18**(12), 7665–7673 (2018).

29. J. Park, J.-H. Kang, X. Liu, S. J. Maddox, K. Tang, P. C. McIntyre, S. R. Bank, and M. L. Brongersma, "Dynamic thermal emission control with InAs-based plasmonic metasurfaces," Sci. Adv. **4**(12), eaat3163 (2018).

30. T. Cao, X. Y. Zhang, W. L. Dong, L. Lu, X. L. Zhou, X. Zhuang, J. H. Deng, X. Cheng, G. X. Li, and R. E. Simpson, "Tuneable Thermal Emission Using Chalcogenide Metasurface," Adv. Opt. Mater. **6**(16), 1800169 (2018).

31. X. Xie, X. Li, M. B. Pu, X. L. Ma, K. P. Liu, Y. H. Guo, and X. G. Luo, "Plasmonic Metasurfaces for Simultaneous Thermal Infrared Invisibility and Holographic Illusion," Adv. Funct. Mater. **28**(14), 1706673 (2018).

32. G. Y. Lu, C. R. Gubbin, J. R. Nolen, T. Folland, M. J. Tadjer, S. De Liberato, and J. D. Caldwell, "Engineering the Spectral and Spatial Dispersion of Thermal Emission via Polariton-Phonon Strong Coupling," Nano Lett. **21**(4), 1831–1838 (2021).

33. Z. Xu, H. Luo, H. Zhu, Y. Hong, W. Shen, J. Ding, S. Kaur, P. Ghosh, M. Qiu, and Q. Li, "Nonvolatile Optically Reconfigurable Radiative Metasurface with Visible Tunability for Anticounterfeiting," Nano Lett. **21**(12), 5269–5276 (2021).

34. A. C. Overvig, S. A. Mann, and A. Alu, "Thermal Metasurfaces: Complete Emission Control by Combining Local and Nonlocal Light-Matter Interactions," Phys. Rev. X **11**(2), 021050 (2021).

35. X. Wang, T. Sentz, S. Bharadwaj, S. K. Ray, Y. Wang, D. Jiao, L. Qi, and Z. Jacob, "Observation of nonvanishing optical helicity in thermal radiation from symmetry-broken metasurfaces," Sci. Adv. **9**(4), eade4203 (2023).

36. K. J. Shayegan, S. Biswas, B. Zhao, S. H. Fan, and H. A. Atwater, "Direct observation of the violation of Kirchhoff's law of thermal radiation," Nat. Photonics **17**(10), 891–896 (2023).

37. A. Lochbaum, Y. Fedoryshyn, A. Dorodnyy, U. Koch, C. Hafner, and J. Leuthold, "On-Chip Narrowband Thermal Emitter for Mid-IR Optical Gas Sensing," ACS Photonics **4**(6), 1371–1380 (2017).

38. B. Liu, W. Gong, B. Yu, P. Li, and S. Shen, "Perfect Thermal Emission by Nanoscale Transmission Line Resonators," Nano Lett. **17**(2), 666–672 (2017).

39. X. Zhang, H. Liu, Z. G. Zhang, Q. Wang, and S. N. Zhu, "Controlling thermal emission of phonon by magnetic metasurfaces," Sci. Rep. **7**(1), 41858 (2017).

40. X. Zhang, Z. G. Zhang, Q. Wang, S. N. Zhu, and H. Liu, "Controlling Thermal Emission by Parity-Symmetric Fano Resonance of Optical Absorbers in Metasurfaces," ACS Photonics **6**(11), 2671–2676 (2019).

41. F. Zhong, K. Ding, Y. Zhang, S. Zhu, C. T. Chan, and H. Liu, "Angle-Resolved Thermal Emission Spectroscopy Characterization of Non-Hermitian Metacrystals," Phys. Rev. Appl. **13**(1), 014071 (2020).

42. Q. Q. Chu, F. Y. Zhang, Y. Zhang, T. Qiao, S. N. Zhu, and H. Liu, "Integrated thermal emission microchip based on meta-cavity array," Nanophotonics **11**(18), 4263–4271 (2022).

43. C. Wu, A. B. Khanikaev, R. Adato, N. Arju, A. A. Yanik, H. Altug, and G. Shvets, "Fano-resonant asymmetric metamaterials for ultrasensitive spectroscopy and identification of molecular monolayers," Nat. Mater. **11**(1), 69–75 (2012).

44. H. Y. Yang, S. N. Yang, J. L. Kong, A. C. Dong, and S. N. Yu, "Obtaining information about protein secondary structures in aqueous solution using Fourier transform IR spectroscopy," Nat. Protoc. **10**(3), 382–396 (2015).

45. F. B. Barho, F. Gonzalez-Posada, M. Bomers, A. Mezy, L. Cerutti, and T. Taliercio, "Surface-Enhanced Thermal Emission Spectroscopy with Perfect Absorber Metasurfaces," ACS Photonics **6**(6), 1506–1514 (2019).

46. K. Nakagawa, Y. Shimura, Y. Fukazawa, R. Nishizaki, S. Matano, S. Oya, and H. Maki, "Microemitter-Based IR Spectroscopy and Imaging with Multilayer Graphene Thermal Emission," Nano Lett. **22**(8), 3236–3244 (2022).